Chinese Journal of
POLYMER SCIENCE

RESEARCH ARTICLE

https://doi.org/10.1007/s10118-023-3006-3
Chinese J. Polym. Sci. **2023**, *41*, 1889–1901

MOF-derived Porous Carbon Nanofiber Assembly as High Efficiency ORR Electrocatalysts for Zinc-air Batteries

Jin-Liang Ma, Long-Long Liu, Ren-Hai Zhao, Ding Yuan*, and Xin Ning*

Industrial Research Institute of Nonwovens & Technical Textiles, Shandong Center for Engineered Nonwovens, College of Textiles & Clothing, Qingdao University, Qingdao 266071, China

Electronic Supplementary Information

Abstract Reasonable construction of high activity and low cost non-noble metal oxygen reduction reaction (ORR) catalyst is of great importance for the wide application of zinc-air batteries (ZABs). Using bimetallic MOF as a precursor combined with electrospinning, high-temperature carbonization and electrodeposition, we successfully developed a porous carbon nanofiber (Co@Fe-CNFs-1000) with bimetallic active center as an efficient catalyst for ORR. The successful construction of this special core-shell structure directly explores the synergy between different active centers. The results showed that the synthesized Co@Fe-CNFs-1000 catalyst exhibited ORR performance comparable to that of Pt/C in 0.1 mol/L KOH electrolyte, high half-wave potential ($E_{1/2}$=0.81 V) and limiting current density (J_L=5.4 mA·cm^{-2}). In addition, homemade liquid ZABs with Co@Fe-CNFs-1000 as the air cathode showed excellent power density (155.8 mW·cm^{-2}), specific capacity (780.6 mAh·g$_{Zn}^{-1}$) and long-term stability (over 100 h at 2 mA·cm^{-2}), surpassing even Pt/C-based batteries. In addition, the flexible solid-state ZABs assembled based on Co@Fe-CNFs-1000 demonstrates excellent flexibility and durability. This work provides a new idea for constructing ORR catalysts with high activity centers.

Keywords Electrospinning; Porous structure; ORR; Bimetallic MOFs; Zinc-air battery

Citation: Ma, J. L.; Liu, L. L.; Zhao, R. H.; Yuan, D.; Ning, X. MOF-derived porous carbon nanofiber assembly as high efficiency ORR electrocatalysts for zinc-air batteries. *Chinese J. Polym. Sci.* **2023**, *41*, 1889–1901.

INTRODUCTION

Continuous energy consumption and environmental degradation have stimulated the development of sustainable energy storage and conversion equipment.[1–5] Zinc-air batteries (ZABs) are attracting increasing attention because of their low cost, high energy density and environmental friendliness.[6–9] However, the relatively slow electrocatalytic reactions involved in battery cathodes, including oxygen reduction reactions (ORR), hinder their direct applications.[10,11] Therefore, it is necessary to design an ideal electrocatalyst to solve the problem of slow ORR kinetics.[12] Although precious metal (Pt) based catalysts are considered as ideal catalysts for ZABs, they have disadvantages such as high cost, poor stability and poor availability, which directly hinder the large-scale application of ZABs.[13–15] In this context, the attention is gradually turning to the design and development of non-precious metal based catalysts, which are essential to promote the high quality development of ZABs.

In previous studies, Fe, N co-doped carbon-based materials (Fe-N_XC) often showed surprising ORR electrocatalytic activity.[16–18] Among them, the synergistic effect of Fe, N and C is realized through element doping, which also regulates the electronic structure of the material and further generates more abundant active sites.[19–21] Fe-N_XC has been considered as one of the promising ORR catalysts, because these active sites enhance the adsorption capacity of oxygen species in transition states and reduce the energy barrier during the reaction.[22–24] The common preparation strategy of Fe-N_XC is based on the pyrolysis of metal-organic skeleton (MOF), because MOF has the advantages of controllable crystal configuration, rich pore structure, and *in situ* nitrogen source.[25–27] However, collapse, structural damage and metal particle aggregation often occur during high temperature pyrolysis of MOF, which will directly reduce the specific surface area and destroy the pore structure, thus affecting the electrocatalytic performance of the catalyst.[26] In order to solve this problem properly, it is an effective reform measure to arrange MOF on conductive carbon matrix in order before high temperature pyrolysis.[27,28] Electrospinning carbon nanofiber materials are considered as effective carbon matrix because of their large surface area and excellent electrical conductivity.[29,30] This material not only solves the waste problem of inorganic template, but also provides a longer electron transport channel.[31] But even so, these materials with only single metal active sites will still show poor durabil-

* Corresponding authors, E-mail: yuanding@qdu.edu.cn (D.Y.)
E-mail: xning@qdu.edu.cn (X.N.)

Received March 29, 2023; Accepted May 26, 2023; Published online July 10, 2023

ity and low activity.[32]

It is well known that introducing Co species to construct core-shell structure is an effective means to improve the electrocatalytic performance of carbon-based materials. This is because bimetallic active sites can be constructed by introducing Co species, which not only regulates the electronic structure of carbon atoms, but also the adsorption energy of intermediates, and finally improves the performance.[33] Many studies also confirmed that there is a synergistic effect between iron species and cobalt species in iron matrix composites, which may be through doping or forming multiple metal compounds to change the electronic structure of the catalyst.[34] On the one hand, iron species can also exert partial charge transfer activation effect on introduced cobalt species. On the other hand, the charge-carrier density and electron conductivity can also be improved with the introduction of cobalt species.[35] Co species tend to exhibit good ORR activity either as nanoparticles or when they are encapsulated in N/C nanostructures (such as carbon nanotubes, porous carbon structures, *etc*.).[36] For example, Xue *et al*. synthesized N-doped porous carbon using MOF as a precursor by in-situ doping, in which Co nanoparticles and Fe-N_X active sites are evenly dispersed on the carbon substrate. The catalyst CoNP@FeNC-0.05 prepared by introducing Co particles showed excellent bi-functional activity.[37] In the study of Zhao *et al*., it was found that porous carbon with bimetallic active center can be synthesized successfully by pre-doping (Co@C/Fe-NC). Among them, Fe species can establish Fe-N_X active sites on the substrate by means of coordination, and Co species can not only transform into nanoparticles at high temperature, but also induce carbon to transform into carbon nanotubes.[38] These special structural characteristics are conducive to the ORR process. In addition, zinc species in MOF can also act as pore-forming agents to disperse metal-based materials in highly porous structures, which facilitates the increase of specific surface area and the full utilization of metal active sites.[39,40] Therefore, the ORR activity of carbon-based electrocatalysts can be effectively improved by constructing bimetallic centers.

For this purpose, Fe-N_XC porous carbon nanofiber substrate was constructed using ZnFe-MOF as precursor, and Co species were loaded onto the substrate by electrodeposition technology. Finally, a high performance ORR catalyst containing Fe-N_XC active sites, Co-N_XC active sites and Co nanoparticles co-exists in hollow porous carbon fibers (Co@Fe-CNFs-1000). In alkaline electrolyte, Co@Fe-CNFs-1000 has the advantages of low half-wave potential (0.81 V), nearly four electron transfer process (3.93), and good stability. Liquid/flexible solid-state ZABs assembled on Co@Fe-CNFs-1000 also have higher power density and excellent stability compared to Pt/C-based batteries. This work could provide a new option for non-precious metal ORR high efficiency catalysts used in sustainable energy storage and conversion equipment.

EXPERIMENTAL

Materials and Chemicals

Zinc nitrate ($Zn(NO_3)_2{\cdot}6H_2O$), cobalt nitrate ($Co(NO_3)_2{\cdot}6H_2O$), ferrous sulfate ($FeSO_4{\cdot}7H_2O$), *N*,*N*-dimethylformamide (DMF), anhydrous methanol (CH_3OH), ethanol (C_2H_5OH), potassium hydroxide (KOH), zinc acetate ($Zn(CH_3COO)_2$) and Nafion solution (5 wt%) were purchased from Sinopharm Chemical Reagent Co., Ltd., Shanghai, China. 2-Methylimidazole (2-MeIM), polyacrylonitrile (PAN, M_w ~1.5×10^5) and poly(vinyl alcohol) (PVA, M_w ~1.95×10^5) were supplied by Aladdin Chemical Co., LTD. Commercial Pt/C (20 wt%) was provided by Meryl Corporation.

Synthesis of Electrocatalysts

Preparation of ZnFe-MOF

Generally, 0.8 mmol $FeSO_4{\cdot}7H_2O$ and 14 mmol $Zn(NO_3)_2{\cdot}6H_2O$ were dissolved ultrasonically in 150 mL of anhydrous methanol to form mixed solution A; 60 mmol 2-MeIM was dissolved in 150 mL of anhydrous methanol to form mixed solution B. Solution B is then slowly added to solution A at room temperature, stirring vigorously. After mixing well, let stand at room temperature for 24 h. Finally, the light yellow solid powder ZnFe-MOF was obtained by centrifugation. After washing with methanol for several times, the powder was dried in the oven at 60 °C for 6 h. The yield of ZnFe-MOF is about 30%.

Preparation of ZnFe-MOF/PAN

ZnFe-MOF (0.4 g) was dispersed in DMF (4.35 g) by ultrasonic action, and then PAN (0.65 g) was added and stirred continuously at room temperature for 36 h. The homogeneous spinning solution was successfully prepared. The nanofiber membrane used in the experiment was manufactured using a homemade electrospinning facility consisting of a high-voltage DC power supply (GAMMA, Washington, DC, USA), an injection pump (LSP02-1B, Baoding Lange Constant Flow Pump Co., Ltd., China) and a drum receiver. Typically, the spinning solution is inhaled into a 5 mL syringe and a metal receiving roller covered with silicone oil paper is used to collect the nanofibers. The applied voltage is 19 kV and the feed rate is 22 μL·min^{-1}. The receiver speed, reception distance, rotation temperature and relative humidity were set at 125 r/min, 20 cm, 25±3 °C and 45%±3%, respectively. In addition, the prepared nanofiber membrane was dried in an oven at 60 °C for 1 h before use to remove the residual solvent to obtain a light yellow solid nanofiber ZnFe-MOF/PAN. The yield of ZnFe-MOF/PAN is close to 20%.

Preparation of Fe-CNFs

The black solid nanofibers were named as Fe-CNFs after annealing with ZnFe-MOF/PAN and heating under 800 °C argon for 2 h. The yield of Fe-CNFs is about 35%.

Preparation of Co@Fe-CNFs

$Co(OH)_2$/Fe-CNFs were prepared by electrochemical deposition. Electrodeposition was performed in a standard three-electrode system at room temperature. With Fe-CNFs as the working electrode, the reference electrode and the reverse electrode were Ag/AgCl (3 mol/L KCl) electrode and platinum wire, respectively. The electrolyte was composed of 2 mmol $Co(NO_3)_2{\cdot}6H_2O$ dissolved in 100 mL of deionized water. Electrodeposition was performed at −1.0 V versus Ag/AgCl for 100, 300, 500 s. The obtained $Co(OH)_2$/Fe-CNFs were then removed from the electrolyte, rinsed three times with deionized water and dried at 60 °C. In addition, Co@Fe-CNFs is synthesized by pyrolysis of $Co(OH)_2$/Fe-CNFs-300s at high temperatures. Specifically, $Co(OH)_2$/Fe-CNFs underwent a 2 h carbonization process under 800, 900 and 1000 °C argon, respectively. The

https://doi.org/10.1007/s10118-023-3006-3

obtained samples at different carbonization temperatures were named Co@Fe-CNFs-800, Co@Fe-CNFs-900, Co@Fe-CNFs-1000. For comparison, $Co(OH)_2$@CNFs was prepared by replacing ZnFe-MOF with ZIF-8 by the similar method described above, and Co@CNFs was synthesized by heating under 1000 °C argon for 2 h. The yield of Co@Fe-CNFs-1000 is close to 85%.

Material Characterization

By scanning electron microscopy (FE-SEM, Regulus8100), energy dispersive X-ray spectroscopy (EDS, Super-X), transmission electron microscopy (TEM, HT7700), raman spectroscopy (Raman, HORIBA Scientific LabRAM HR Evolution), X-ray diffraction (XRD, Rigaku MiniFlex600) characterized the morphology and structure of the catalyst. N_2 adsorption/desorption isotherms were obtained using Quantachrome-EVO surface area and porosity analyzer. The surface composition and chemical state of the samples were studied by X-ray photoelectron spectroscopy (XPS). An inductively coupled plasma optical emission spectrometer (ICP-OES, Agilent730) was used.

Electrochemical Measurements

Electrochemical performance was tested using the standard three-electrode apparatus of the CHI 760E and rotating disk electrode (RDE). The glassy carbon electrode (4 mm in diameter) coated with a catalyst sample, Hg/HgO electrode and platinum wire as the working electrode, reference electrode and the counter electrode, respectively. The measured potential was corrected by Nernst equation $E_{RHE} = E_{Hg/HgO} + 0.059pH + 0.098$. In order to prepare the working electrode, catalyst ink is prepared. The catalyst ink was composed of 5 mg of prepared catalyst, 485 μL of ethanol, 485 μL of deionized water and 30 μL of Nafion solution (5 wt%), which was formed after ultrasonic treatment for 60 min. Finally, 5 μL of ink was dropped onto the polished glass carbon electrode and air dried. Under the same conditions, commercial Pt/C (20 wt%) catalyst was prepared for reference. For ORR tests, samples were tested for the catalyst CV curve in an N_2- and O_2-saturated 0.1 mol·L^{-1} KOH electrolyte of 0–1.2 V versus RHE at a scanning rate of 50 mV·s^{-1}. Linear sweep voltammetry (LSV) curves were measured at 0.1 mol·L^{-1} KOH saturated with O_2 at a sweep rate of 10 mV·s^{-1} and analyzed at speeds between 400 and 2025 r·min^{-1}. The Tafel slope can be calculated by the Tafel equation:[41]

$$\eta = a + b\log(j) \tag{1}$$

where η, j and b represent overpotential, current density, and Tafel slope, respectively.

The number of electrons (n) transferred by oxygen reduction can be analyzed by Koutecky-Levich (K-L) equation:[42,43]

$$\frac{1}{J} = \frac{1}{J_k} + \frac{1}{J_L} = \frac{1}{J_k} + \frac{1}{B\omega^{\frac{1}{2}}} \tag{2}$$

$$B = 0.2nFC_0D_0^{2/3}v^{-1/6} \tag{3}$$

where J is the measured current density, J_k and J_L are the kinetic limit current density and the diffusion limit current density respectively. F is the Faraday constant (96485 C·mol^{-1}), ω is the electrode speed, and n is the number of electron transfers per oxygen molecule. D_0 is the diffusion coefficient of O_2 (1.9×10^{-5} cm^2·s^{-1}), C_0 is the volume concentration of O_2 (1.2×10^{-6} mol·cm^{-3}), v is the kinematic viscosity of the electrolyte (0.1 mol·L^{-1} KOH, 0.01 cm^2·s^{-1}).

The long-term stability of the prepared catalyst was tested at 0.6 V versus RHE by constant-current test in O_2-saturated 0.1 mol·L^{-1} KOH at a rotational speed of 1600 r·min^{-1}. At the same time, the methanol tolerance of the samples was tested by adding 5% methanol to the electrolyte under the same conditions.

The rotating ring-disk electrode (RRDE) test was performed at a scan rate of 10 mV·s^{-1} and rotation speed rate of 1600 r·min^{-1} in O_2-saturated 0.1 mol·L^{-1} KOH. The potential of the Pt ring was set to 1.365 V versus RHE to test the ring current (I_r). Peroxide yield (H_2O_2%) and electron transfer number (n) can be calculated by the following equations:[44]

$$n = 4 \times \frac{i_d}{\frac{i_r}{N} + i_d} \tag{4}$$

$$H_2O_2\,(\%) = 200 \times \frac{\frac{i_r}{N}}{\frac{i_r}{N} + i_d} \tag{5}$$

where i_d and i_r are disk current and ring current respectively, N is the collection efficiency of ring current (N=0.47).

In addition, electrochemical impedance spectroscopy (EIS) was measured in the frequency range from 0.01 Hz to 1000 kHz with an amplitude of 5 mV.

Liquid and Flexible Solid-State ZABs Assembly

Zinc-air batteries consist of three parts: anode, electrolyte and cathode. We have assembled both liquid and flexible solid-state ZABs. For the liquid zinc-air battery, a new polished zinc plate with a thickness of 0.2 mm was selected as the anode, liquid electrolyte was prepared by dissolving 6 mol·L^{-1} KOH and 0.2 mol·L^{-1} $Zn(Ac)_2$ in water. Air cathode was prepared by coating catalyst (1 mg·cm^{-2}) on carbon paper/gas diffusion layer mixed electrode. Specifically, 200 μL of catalyst ink was titrated on carbon paper with an area of 1 cm^{-2}. Preparation of catalyst inks is the same as in electrochemical measurement. For flexible solid-state ZABs, thin and flexible zinc plates were selected as the anode, commercial carbon cloth supported catalyst ink as the cathode, and PVA gel electrolyte as the solid electrolyte. The gel electrolyte was prepared by adding 2 g of PVA powder to 20 mL of 6.0 mol·L^{-1} KOH solution containing 0.2 mol·L^{-1} $Zn(CH_3COO)_2$ and stirring at 90 °C until the solution was uniform. Then, pour the above solution into a square glass container, form a film of about 1 mm and put it in the refrigerator, and thaw it at room temperature after 12 h. As a reference, the battery was assembled using a commercial Pt/C (20 wt%) catalyst under the same conditions. In addition, the open-circuit voltage and power density of the ZABs were measured at an electrochemical workstation (CHI 760E), where the polarization curve was acquired at a scan rate of 10 mV·s^{-1}. The specific capacity was calculated by the zinc plate consumption recorded by the LAND BT2018R multichannel battery test system during continuous discharge at current densities of 10 and 2 mA·cm^{-2}, respectively. Meanwhile, the discharge-charge cycle stability of the assembled zinc-air batteries was tested at the current densities of 2 and 1 mA·cm^{-2}, respectively.

RESULTS AND DISCUSSION

Scheme 1 depicts a multi-step synthesis strategy for Co@Fe-

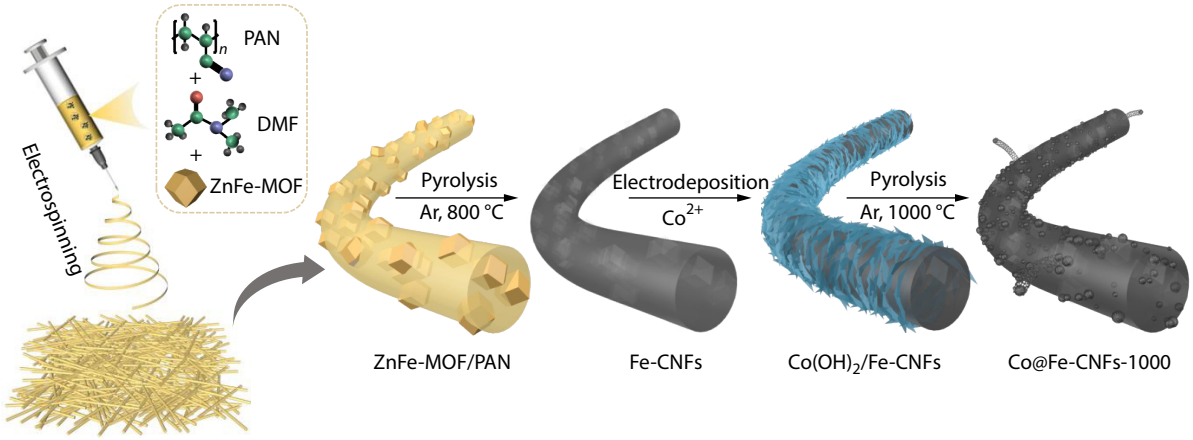

Scheme 1 Schematic illustration of the preparation for Co@Fe-CNFs-1000.

CNFs-1000, including ZnFe-MOF synthesis, electrospinning and post-processing. First, ZnFe-MOF was synthesized by solution method, and the crystal structure of the synthesized particles was analyzed by X-ray diffraction spectroscopy (XRD). The results show that the diffraction peaks of ZnFe-MOF are highly consistent with those previously reported (Fig. S1 in the electronic supplementary information, ESI).[45] Next, ZnFe-MOF/PAN was prepared by electrospinning by mixing the PAN and the obtained ZnFe-MOF uniformly, which successfully wrapped ZnFe-MOF in PAN nanofibers. Selecting polyacrylonitrile (PAN) as the substrate for electrospinning fibers can maintain one-dimensional structure and prevent the aggregation of nanoparticles during pyrolysis.[46] Then, Fe-CNFs were obtained by annealing the membrane at 800 °C for 2 h. A layer of $Co(OH)_2$ nanosheets was coated on the surface of Fe-CNFs by subsequent electrodeposition process. Finally, the prepared $Co(OH)_2$/Fe-CNFs were transformed into Co@Fe-CNFs one-dimensional porous carbon nanofibers (denoted as Co@Fe-CNFs-Ts, T denotes carbonation temperature) by heat treatment under argon atmosphere at different temperatures (800–1000 °C) for 2 h.

The morphologies of the samples were characterized by scanning electron microscopy (SEM) and transmission electron microscopy (TEM). Fig. 1(a) shows the morphology of PAN fibers, whose surface is smooth and whose diameter is in the range of 200–300 nm. The surface of the nanofibers became rough after the addition of ZnFe-MOF particles (Fig. 1b), indicating that ZnFe-MOF was successfully introduced into PAN fibers (mean diameter of about 900 nm). The uniform dispersion of MOF in PAN nanofibers promotes the uniform distribution of metals and nitrogen in the derived carbon matrix.[47] SEM images of ZnFe-MOF/PAN held in argon at 800 °C for 2 h (Figs. 1c and 1d) indicate that Fe, N co-doped porous carbon nanofibers (Fe-CNFs) have been prepared successfully. It can be seen that the basic morphology of the fiber is maintained after high temperature carbonization, but the fiber diameter shrinks to about 500 nm. At the same time, due to the pyrolysis of ZnFe-MOF, a large number of pore structures and carbon defects are evenly distributed in the fibers.[48]

Then, a simple electrodeposition method was used to modify $Co(OH)_2$ nanosheets onto Fe-CNFs. SEM images showed the $Co(OH)_2$/Fe-CNFs synthesized by Fe-CNFs after different electrodeposition time. If the electrodeposition time is as short as 100 s, the fiber surface changes little. Because in such a short electrodeposition time, uniform $Co(OH)_2$ lamellar structure cannot be formed on the fiber surface (Figs. S2a and S2b in ESI). However, the morphology of $Co(OH)_2$/Fe-CNFs samples changes with the increase of electrodeposition time. As the electrodeposition time increases to 300 s (Figs. 1e and 1f), a uniform and dense nanosheet structure appears on the surface of the fibers. When the electrodeposition time was continuously increased to 500 s (Figs. S2c and S2d in ESI), it is clear that the nanosheet size on the fiber surface increases due to agglomeration, even covering most of the original pore structure of the fiber. Therefore, the $Co(OH)_2$/Fe-CNFs sample formed at 300 s electrodeposition time was selected as the main experimental object in the subsequent experiment.

Finally, the $Co(OH)_2$/Fe-CNFs were transformed into porous carbon nanofibers Co@Fe-CNFs-1000 by high temperature treatment (Figs. 1g and 1h). Many uniform nanoparticles and a small number of carbon nanotubes were clearly observed along the length direction of the nanofibers. It was preliminarily confirmed that the $Co(OH)_2$ nanosheets were transformed into Co nanoparticles after high temperature treatment, and Co nanoparticles could catalyze the formation of carbon nanotubes at high temperature.[49]

As shown in Figs. 2(a) and 2(b), TEM images clearly show that Co@Fe-CNFs-1000 is a hollow nanofiber structure with a large number of pores evenly distributed on the surface and inside of the fibers. It is also confirmed that Co nanoparticles exist not only on the surface of carbon fiber, but also encased in carbon matrix. The average diameter of the particles is about 15 nm. In addition, a small number of carbon nanotubes with a diameter of about 20 nm are anchored to the surface of the fibers. The uniform distribution of cobalt nanoparticles and pore structure in Co@Fe-CNFs-1000 improves electronic and mass conductivity, which effectively promotes ORR activity.[50] The high-resolution TEM (HRTEM) image in Fig. 2(c) shows lattice streaks with spacing of 0.204 and 0.342 nm, corresponding to the (111) plane of metallic Co and the (002) plane of graphitic carbon, respectively, which is catalyzed by cobalt metal at high temperatures.[51] The structure

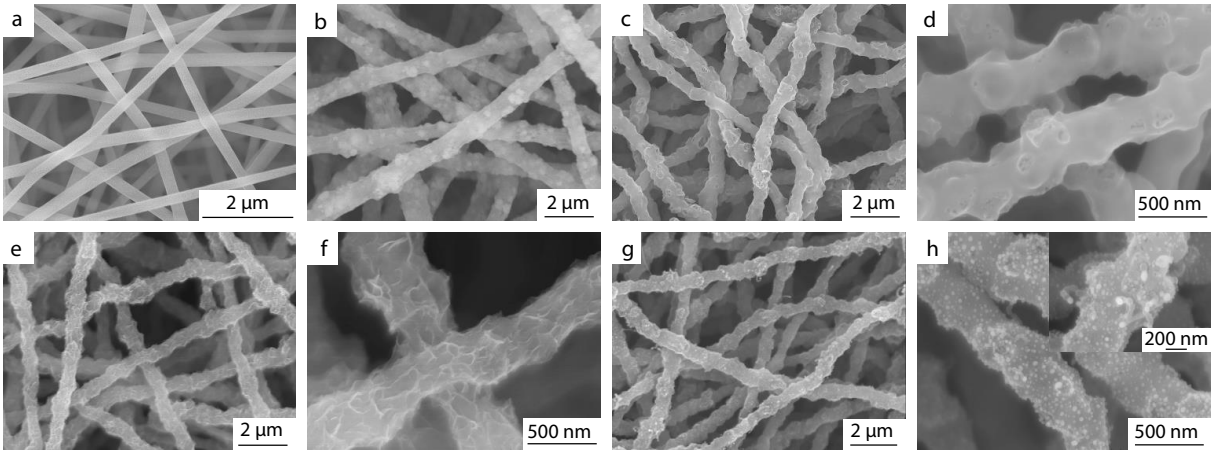

Fig. 1 SEM images of (a) PAN nanofibers, (b) ZnFe-MOF/PAN nanofibers, (c, d) Fe-CNFs nanofibers, (e, f) $Co(OH)_2$/Fe-CNFs nanofibers and (g, h) Co@Fe-CNFs-1000 nanofibers.

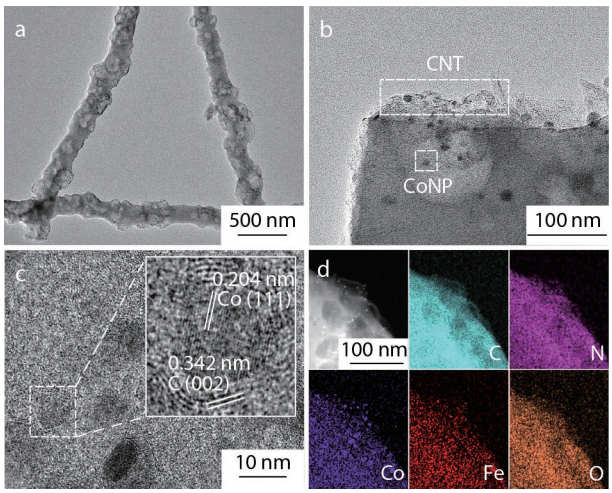

Fig. 2 (a, b) TEM images, (c) HRTEM image, and (d) elemental mapping images of Co@Fe-CNFs-1000.

of the metallic Co nanoparticles surrounded by graphite carbon shell can prevent oxidation and corrosion of Co nanoparticles.[47] In addition, there is a certain synergistic effect between cobalt and graphitic carbon in the electrocatalytic process.[50] Notably, no lattice fringe corresponding to the type of Fe was observed, indicating that Fe atoms did not aggregate to form Fe nanoparticles during the pyrolysis process, which may be due to the combination of Fe atoms with nitrogen.[52] The elemental mapping images show that Co, Fe, C, N and O are uniformly distributed in the pyrolysis product Co@Fe-CNFs-1000 (Fig. 2d). In addition, the element content of Co@Fe-CNFs-1000 was tested by inductively coupled plasma optical emission spectrometer (ICP-OES), and the contents of Co and Fe were 4.05 wt% and 2.14 wt%, respectively (Table S1 in ESI).

As shown in Fig. 3(a), the Fe-CNFs and Co@Fe-CNFs-1000 samples were characterized by X-ray diffractometer (XRD) to verify their composition and crystal structure. A wide diffraction peak is observed at about 26.3° for both samples, corresponding to the (002) plane of graphitic carbon (JCPDS No.41-1487), indicating that the samples had a good degree of graphitization.[44] In addition, relative to the sample Fe-CNFs, Co@Fe-CNFs-1000 also shows diffraction peaks at 44.2°, 51.5° and 76.0°, corresponding to the (111), (200), and (220) planes of metal Co (JCPDS No.15-0806), respectively.[47] The presence of metallic Co nanoparticles was again confirmed. However, no diffraction peaks belonging to iron species can be observed in the Co@Fe-CNFs-1000 sample, which is consistent with HRTEM. Raman spectroscopy was used to evaluate the degree of graphitization of each sample (Fig. 3b). The results show that all samples have two significant broad bands at ~1350 and ~1580 cm^{-1}, which represent the defect induced band (D band) and graphite induced band (G band) carbon, respectively.[53] Generally, the peak intensity ratio (I_D/I_G) of D band and G band is used to evaluate the degree of graphitization of carbon materials. In addition, the lower the I_D/I_G value, the higher the degree of graphitization of the measured sample.[54] The results show that the I_D/I_G value (1.01) of Co@Fe-CNFs-1000 is lower than that of other samples (Co@CNFs was 1.08, Fe-CNFs was 1.02), which fully indicated that the degree of graphitization of Co@Fe-CNFs-1000 was improved. It is beneficial to strengthen the conductivity and corrosion resistance of the catalyst in the electrocatalysis process, which is consistent with the X-ray diffraction test results.[51]

The specific surface area and pore structure of Fe-CNFs, Co@CNFs and Co@Fe-CNFs-1000 were evaluated by nitrogen adsorption-desorption techniques (Fig. 3c). Obviously, the nitrogen adsorptions-desorption curves of Co@Fe-CNFs-1000 exhibit type IV isotherms. Steep slopes at low relative pressures indicate that the product has a microporous structure, while obvious hysteresis curves at relative pressures between 0.4 and 0.9 indicate that the material has a mesoporous structure.[55] This conclusion is also proved in the illustration of Fig. 3(c). In addition, Co@Fe-CNFs-1000 has a specific surface area of 311.8 $m^2 \cdot g^{-1}$, higher than Fe-CNFs (259.9 $m^2 \cdot g^{-1}$) and slightly lower than Co@CNFs (376.1 $m^2 \cdot g^{-1}$). Although the large surface area and the coexistence of micropores and mesoporous can promote rapid diffusion and mass transfer and accelerate oxygen reduction processes, the synergistic behavior between metals makes Co@Fe-CNFs-1000 catalysts dominant in ORR electrocatalysis.[56]

https://doi.org/10.1007/s10118-023-3006-3

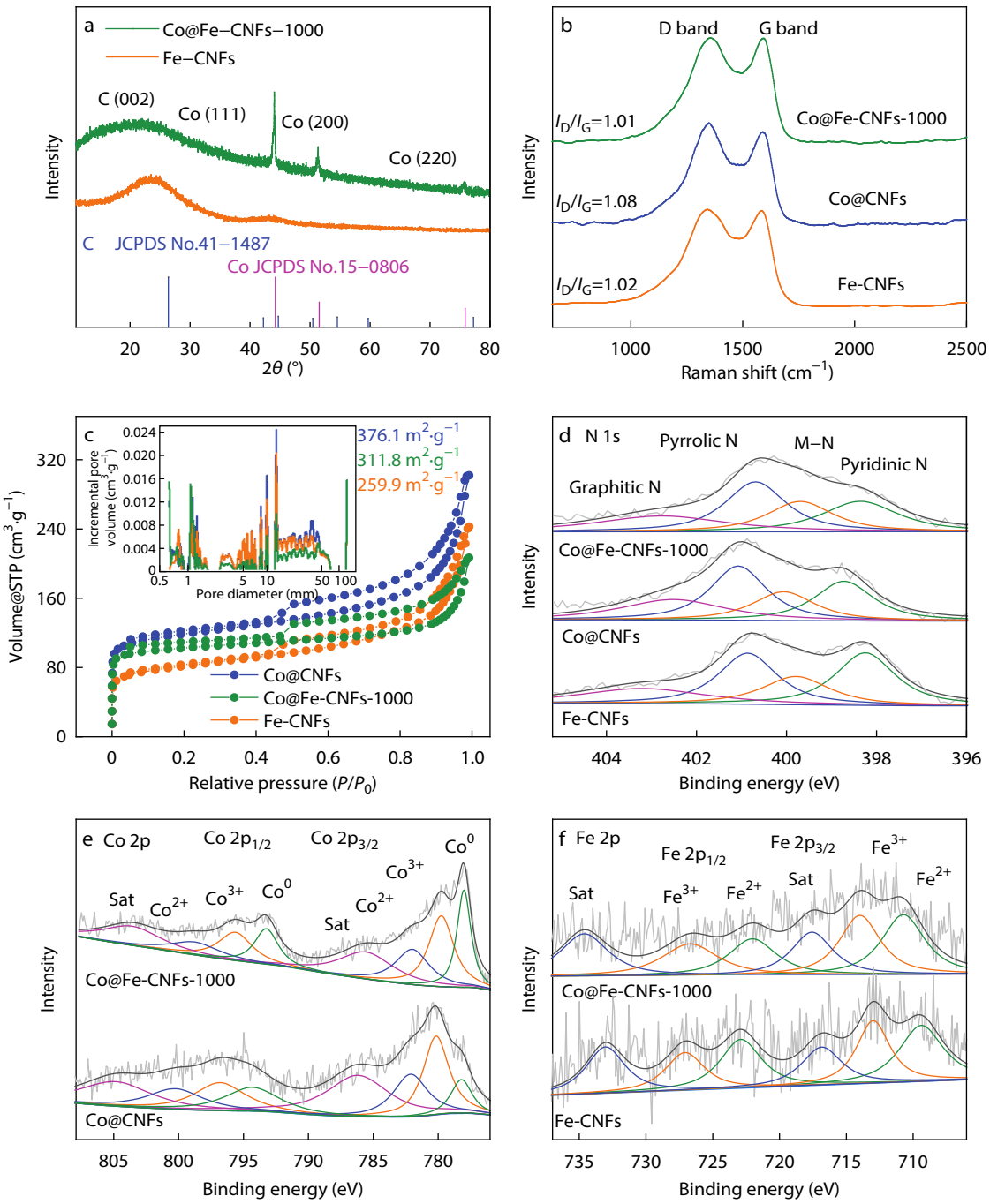

Fig. 3 (a) XRD patterns of Fe-CNFs and Co@Fe-CNFs-1000; (b) Raman spectra of Fe-CNFs, Co@CNFs and Co@Fe-CNFs-1000; (c) N_2 adsorption/desorption isotherm of all samples, the inset image displays the corresponding pore size distribution curve; High-resolution XPS spectra of (d) N 1s, (e) Co 2p, and (f) Fe 2p for related samples.

The chemical compositions and valence states of related elements in Co@Fe-CNFs-1000, Co@CNFs and Fe-CNFs samples were analyzed by XPS. The measured spectra show that Co, Fe, C, N and O species exist in Co@Fe-CNFs-1000. Co, C, N and O species exist in Co@CNFs; Fe, C, N, and O species species are present in Fe-CNFs (Fig. S3a in ESI). Fig. S3(b) (in ESI) shows that the high-resolution deconvolved spectrum of C 1s can be divided into three peaks corresponding to sp^2 carbon, C—N/C=N and O—C=O bonds, respectively. The corresponding binding energies are 284.3, 285.5 and 289.6 eV.[41] The presence of C—N/C=N also indicates the successful doping of N.[37] N 1s spectra of all samples show that the nitrogenous species consist of the following four components: pyridinic N (398.4 eV), M—N (399.7 eV), pyrrolic N (400.7 eV), and graphitic N (402.8 eV) species (Fig. 3d).[27] It has been suggested that these N defects with strong coordination ability can be used to anchor metal nanoparticles.[24] In high-resolution Co 2p spectral (Fig. 3e), the two peaks at 778.1 and 793.1

eV correspond to elemental Co, which verifies the existence of Co element mainly in the form of metallic elemental, which is very consistent with TEM and XRD test results.[30] The peaks at 779.8 and 795.4 eV are attributable to Co^{3+} and are accompanied by two satellite belts at 785.4 and 803.2 eV, while the peaks at 782.0 and 798.4 eV correspond to Co^{2+}, indicating the presence of Co-N_XC.[11] In addition, the Fe 2p spectrum in Fig. 3(f) can be fitted to six peaks, respectively ascribed to Fe^{2+} (710.7 and 722.0 eV), Fe^{3+} (714.0 and 726.7 eV) and satellite peaks (717.6 and 734.6 eV), indicating that Fe atoms in Fe-N_XC are mainly in bivalent and trivalent states. This is due to the coordination of Fe with N.[7]

To evaluate the ORR electrocatalytic performance of the prepared catalysts, CV curves of the samples were tested at N_2- and O_2-saturated 0.1 mol/L KOH electrolytes (Fig. 4a). All the prepared catalysts showed obvious oxygen reduction peaks in 0.1 mol·L^{-1} KOH electrolyte saturated with O_2, but these reduction peaks did not exist in nitrogen environment, indicating that these catalysts had certain ORR catalytic activity.[14] In addition, the peak potential of Co@Fe-CNFs-1000 (0.74 V) is better than other catalysts, which also proves that Co@Fe-CNFs-1000 has the highest ORR activity among these catalysts. Linear sweep voltammetry (LSV) of different catalysts were then obtained at 1600 rpm on a rotating disk electrode (RDE) and compared with commercial Pt/C catalysts to further evaluate their ORR activity. As shown in Figs. 4(b) and 4(c), Co@Fe-CNFs-1000 showed excellent ORR activity, with higher E_{onset} of 0.88 V and half-wave potential of 0.81 V ($E_{1/2}$). It is also superior to Co@CNFs (0.84 V, 0.76 V), Fe-CNFs (0.87 V, 0.78 V), CNFs (0.88 V, 0.75 V), and comparable to commercial Pt/C (0.91 V, 0.81 V). At the same time, we found that the ORR performance of Co@Fe-CNFs-1000 was better than that of Co@CNFs and Fe-CNFs, indicating that there is a certain synergistic effect between Co nanoparticles, Co-N_XC and Fe-N_XC. In addition, the influence of temperature on the catalytic activity of ORR was also compared (Fig. S4 in ESI). Compared with Co@Fe-CNFs-800 and Co@Fe-CNFs-900 catalysts, Co@Fe-CNFs-1000 showed the best catalytic activity of ORR.

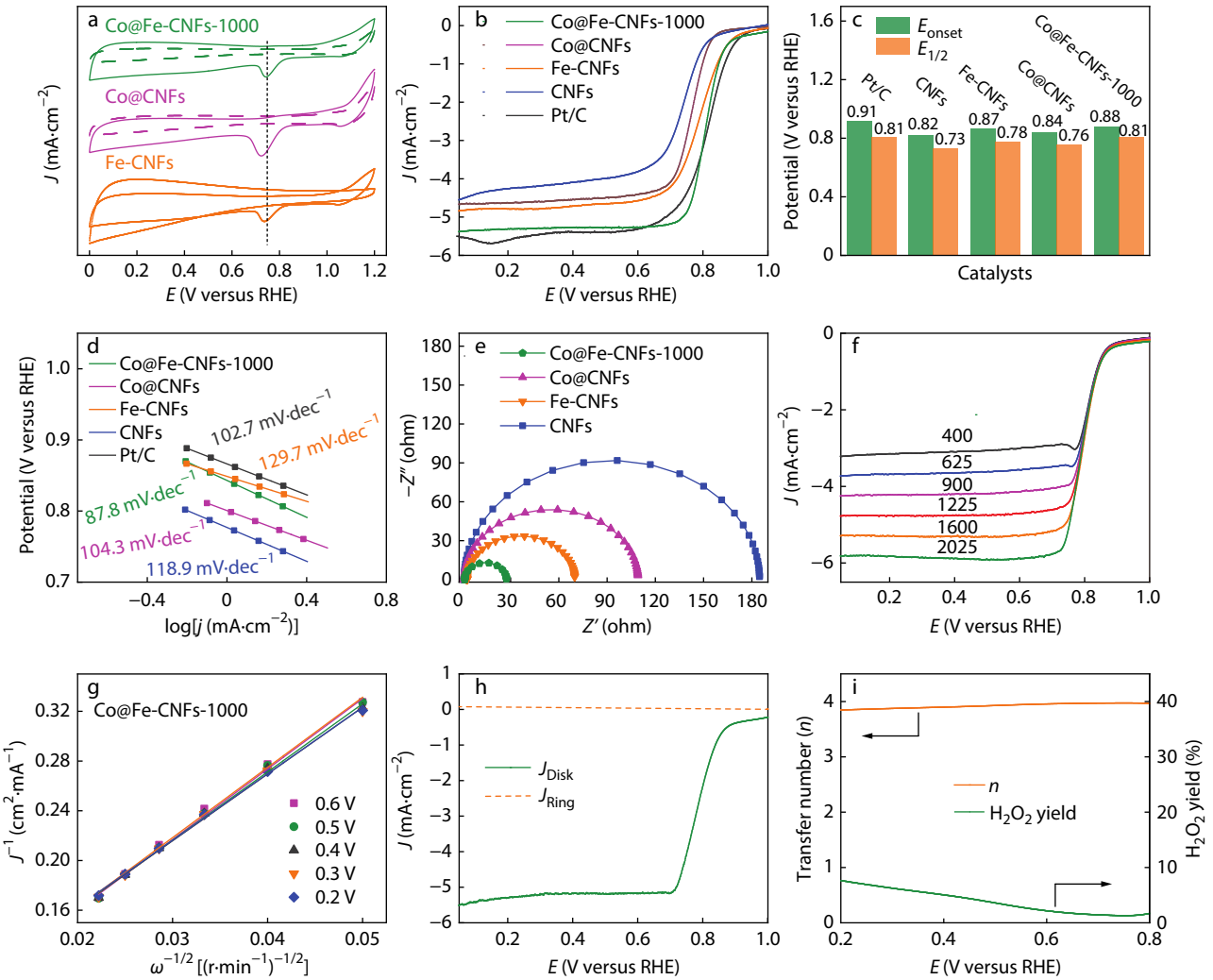

Fig. 4 (a) CV curves of samples in N_2- and O_2-saturated 0.1 mol·L^{-1} KOH electrolyte with 50 mV·s^{-1}; (b) ORR polarization profiles of the samples in a 0.1 mol·L^{-1} KOH solution; (c) The initial potential and half wave potential of each sample; (d) Corresponding Tafel plots; (e) Corresponding Nyquist plots; (f) LSV curves of Co@Fe-CNFs-1000 at different rotation speeds (400–2025 r·min^{-1}) and (g) the K-L plots at different potentials. RRDE curves (h) and the corresponding electron transfer number and H_2O_2 yield (i) of Co@Fe-CNFs-1000.

https://doi.org/10.1007/s10118-023-3006-3

The reaction kinetics of the prepared catalyst was investigated by calculating the Tafel slope. As shown in Fig. 4(d), the corresponding Tafel slope of Co@Fe-CNFs-1000 catalyst is 87.82 mV·dec^{-1}. It is lower than Co@CNFs (104.31 mV·dec^{-1}), Fe-CNFs (129.78 mV·dec^{-1}), CNFs (118.95 mV·dec^{-1}) and Pt/C (108.7 mV·dec^{-1}), indicating the best ORR dynamics. In addition, the reaction kinetics data of these catalysts were characterized by electrochemical impedance spectroscopy (EIS). The Nyquist diagram fitted using an equivalent circuit (Fig. S5 in ESI) is shown in Fig. 4(e). The sample Co@Fe-CNFs-1000 has a much smaller semicircles than the other electrocatalysts, which means that Co@Fe-CNFs-1000 has a smaller charge-transfer resistance than Co@CNFs, Fe-CNFs, and CNFs. The results show that Co@Fe-CNFs-1000 has the strongest charge transfer ability and the fastest electron transport kinetics in ORR process.

To further explore the kinetics, measurements were made using a rotating disk electrode (RDE) in a solution of 0.1 mol/L KOH saturated with O_2. Linear sweep voltammetry (LSV) polarization curves of the sample at Co@Fe-CNFs-1000 at various rotational speeds from 400 r·min^{-1} to 2025 r·min^{-1} were recorded. Fig. 4(f) shows that the limiting current density of Co@Fe-CNFs-1000 increases with the increase of rotational speed, indicating that the oxygen reduction process is a dynamic controlled process.[13] The linearity of the Koutecky-Levich (K-L) curve and the approximate parallelism of the fitting lines indicate the first-order reaction kinetics (Fig. 4g).[43] The RRDE technology was used to further explore the electron transfer kinetics and pathways (Figs. 4h and 4i), the electron transfer number (*n*) and peroxide yield (H_2O_2%) were calculated based on the ring current and disk current. The electron transfer number range of Co@Fe-CNFs-1000 is 3.84–3.96 at a potential of 0.2–0.8 V, and the hydrogen peroxide production range is 1.7%–7.6%, which further proves that Co@Fe-CNFs-1000 mainly follows the ideal four-electron path and the main reduction product is OH^-.

In addition to high electrocatalytic activity, the stability of the catalyst is another important index when considering its practical application. Fig. 5(a) assesses methanol tolerance of Co@Fe-CNFs-1000 and commercially available Pt/C catalysts. After methanol was injected into an O_2-saturated 0.1 mol/L KOH solution, the current density of Co@Fe-CNFs-1000 remained basically unchanged, while the current density of Pt/C catalyst dropped sharply to 58%, indicating that Co@Fe-CNFs-1000 was more tolerant to methanol than Pt/C. The stability of Co@Fe-CNFs-1000 and commercially available Pt/C electrocatalysts was evaluated by chronoamperometric measurements (Fig. 5b). Co@Fe-CNFs-1000 maintained a current density of up to 94%, superior to the Pt/C (20 wt%) catalyst (which retained about 82%), showing its excellent stability. In

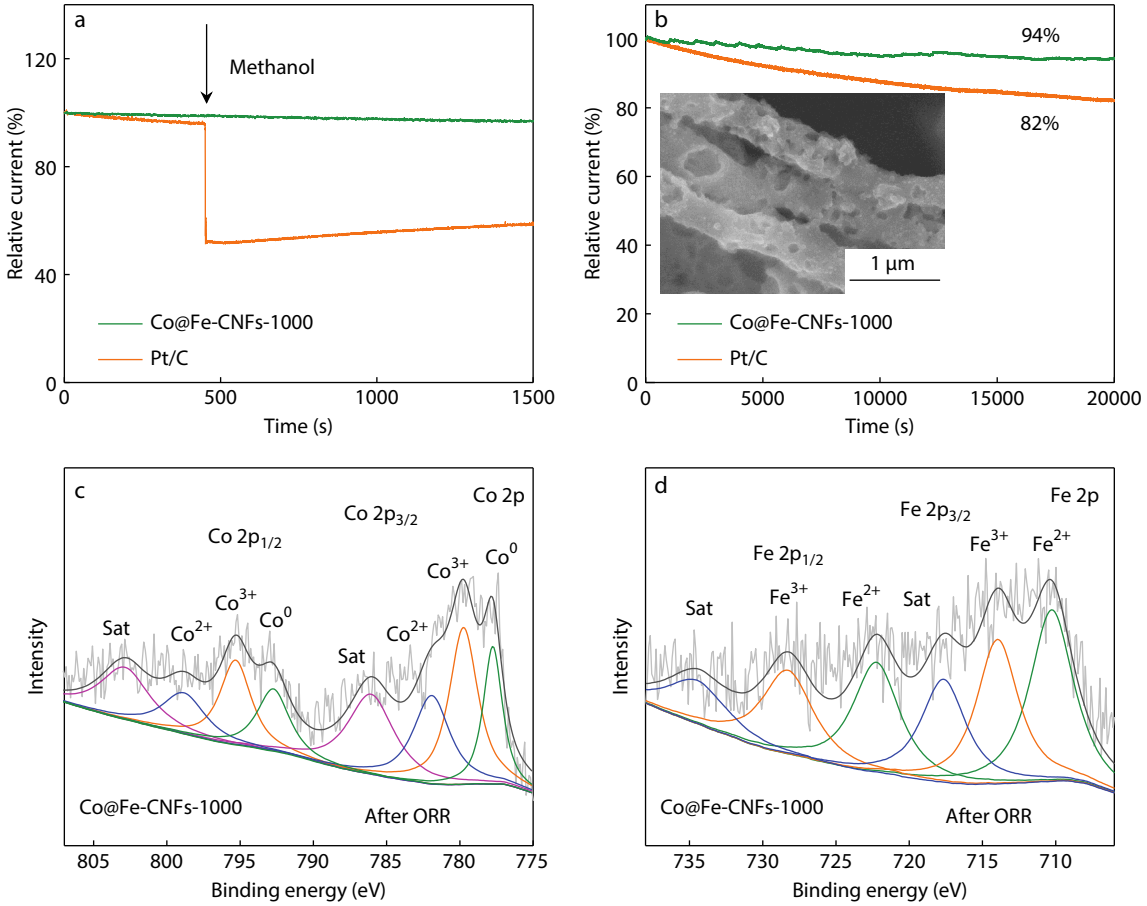

Fig. 5 (a) *I-t* chronoamperometric response of Co@Fe-CNFs-1000 and Pt/C with addition of methanol; (b) Chronoamperometric response of Co@Fe-CNFs-1000 and Pt/C at 1600 r·min^{-1} for 20000 s, the inset image displays the SEM image after stability measurement; (c, d) XPS spectra of Co 2p and Fe 2p for Co@Fe-CNFs-1000 after stability measurement.

https://doi.org/10.1007/s10118-023-3006-3

addition, SEM images of Co@Fe-CNFs-1000 after long-term stability test were observed in the illustration of Fig. 5(b). After the reaction, the basic morphology of the sample was maintained, while the hollow porous structure was exposed. To further explore the structural changes, the Co 2p and Fe 2p XPS spectra of the samples were also measured after long-term stability tests (Figs. 5c and 5d), which showed no significant changes in sample composition.

Inspired by the remarkable electrocatalytic activity of Co@Fe-CNFs-1000 catalyst on ORR, we used it to assemble ZABs. In Fig. 6(a), a liquid ZAB was assembled using a catalyst modified carbon paper as an air cathode, a polished zinc plate as an anode and a mixture of zinc acetate (0.2 mol·L^{-1}) and KOH (6.0 mol·L^{-1}) as an alkaline electrolyte to demonstrate its practical application. Fig. 6(b) shows an open-circuit voltage (OCV) of 1.48 V for the assembled ZABs based on Co@Fe-CNFs-1000, consistent with multimeter tests and slightly higher than for a commercial-Pt/C catalyst driven battery (OCV=1.44 V). As shown in Fig. 6(c), the ZABs assembled with Co@Fe-CNFs-1000 as the cathode catalyst achieves a maximum power density of 155.8 mW·cm^{-1} at 238.2 mA·cm^{-2}. Higher than those assembled using commercial catalyst Pt/C (129.66 mW·cm^{-2} at 205.3 mA·cm^{-2}). We also compared OCV and power density with catalysts recently reported for liquid ZABs (Table S2 in ESI). It can be observed from Fig. 6(d) that the specific capacity of the Co@Fe-CNFs-1000-based battery is up to 780.6 mAh·g$_{Zn}^{-1}$ (based on the consumed weight of the zinc plate) at a discharge current density of 10 mA·cm^{-2}, slightly better than that of the Pt/C-based battery (694.6 mAh·g$_{Zn}^{-1}$). In order to understand how the discharge potential changes with the increase of current density, the constant current discharge measurement was carried out on the assembled ZABs. The Zinc-air battery based on Co@Fe-CNFs-1000 is slightly higher than the Pt/C-based Zinc-air battery at each discharge platform with discharge current density (Fig. 6e), indicating that the Co@Fe-CNFs-1000-based battery

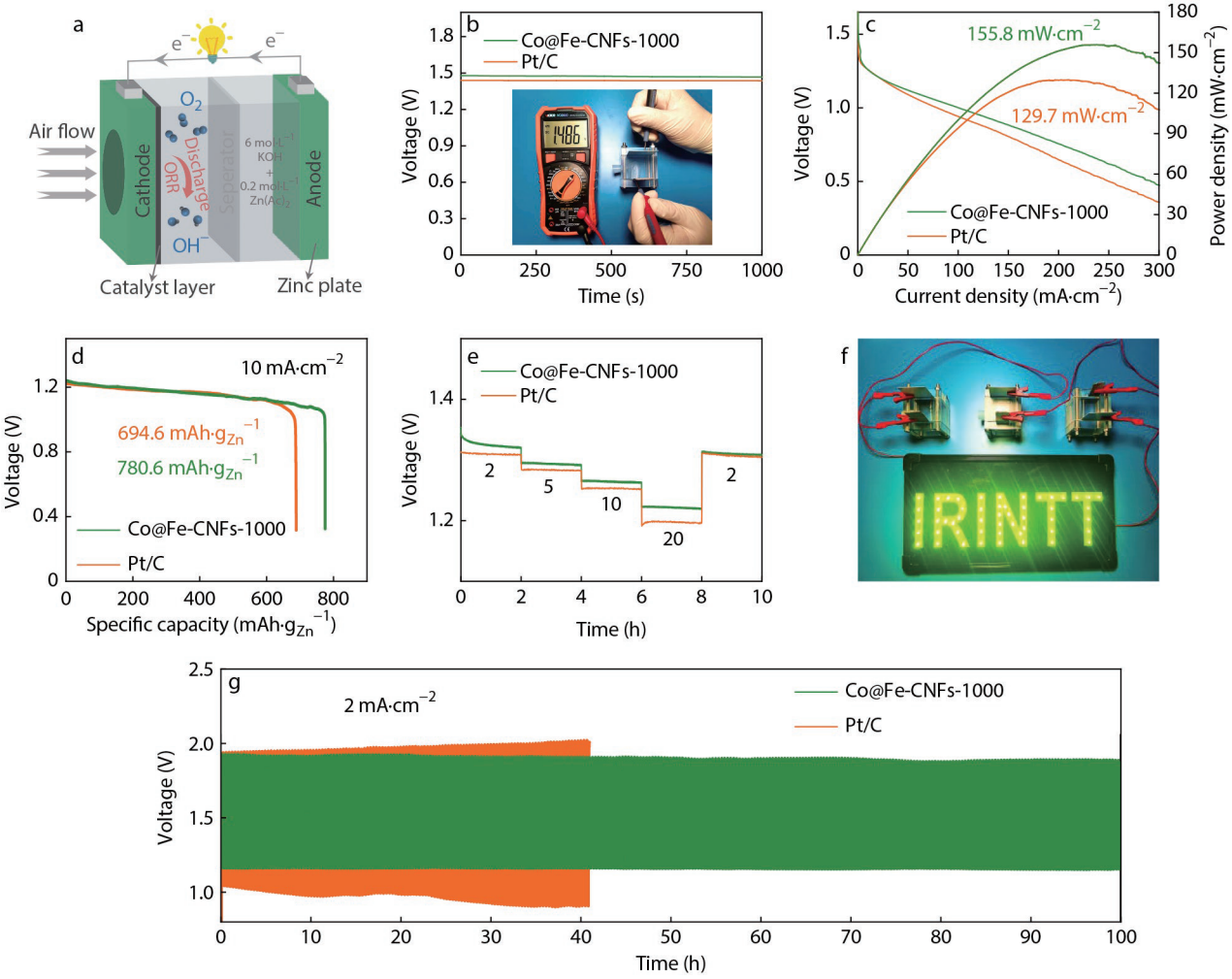

Fig. 6 (a) Schematic diagram of zinc-air battery; (b) Open-circuit voltage curves of ZABs using Co@Fe-CNFs-1000, and Pt/C air cathodes (inset: photograph of Co@Fe-CNFs-1000-based battery); (c) Discharging polarization curves and the corresponding power density curves for batteries employing Co@Fe-CNFs-1000 and Pt/C catalysts; (d) Specific capacity curves of Zinc-air batteries using Co@Fe-CNFs-1000 and Pt/C as air electrodes with a galvanostatic of 10 mA·cm^{-2}; (e) Discharge curves under different current densities; (f) The photograph of a green LED lights powered by three zinc-air batteries in series with Co@Fe-CNFs-1000 as the air-cathode; (g) Cycling stability of rechargeable zinc-air batteries with Co@Fe-CNFs-1000 and Pt/C as the air electrode, respectively.

https://doi.org/10.1007/s10118-023-3006-3

has better discharge rate performance and good reversibility. As shown in Fig. 6(f), the LED panel with an operating voltage of about 4.0 V can be lit by three Co@Fe-CNFs-1000-based batteries connected in series. In addition, in order to evaluate the stability of the Co@Fe-CNFs-1000-based battery, a cyclic charge-discharge test was conducted at 2 mA·cm^{-2} current density. As shown in Fig. 6(g), the Co@Fe-CNFs-1000-based battery maintains a stable voltage gap (1.02 V) throughout the 100-h cycle. However, the charging and discharging voltages of Pt/C-based batteries fluctuate rapidly with the test time under the same conditions. This demonstrates the strong stability of Co@Fe-CNFs-1000 catalyst, consistent with the results of ORR tests.

We have also attempted flexible solid-state ZABs assembled from a carbon cloth supported catalyst Co@Fe-CNFs-1000 as an air cathode, a PVA-KOH gel and a zinc plate as an electrolyte and anode (Fig. 7a). In Fig. 7(b), the flexible solid-state ZABs with Co@Fe-CNFs-1000 catalyst shows an open-circuit voltage of 1.42 V, slightly higher than Pt/C (1.37 V). Fig. 7(c) compares the discharge polarization and corresponding power density curves of solid ZABs based on different cathodes. The peak power density of Co@Fe-CNFs-1000-based battery is about 71.5 mW·cm^{-2} at the current density of 112.7 mA·cm^{-2}, slightly higher than that of the battery using Pt/C as the air cathode (about 53.5 mW·cm^{-2} at the current density of 82.9 mA·cm^{-2}). Then, we compare OCV and power density with catalysts recently reported for flexible solid-state ZABs (Table S3 in ESI). As shown in Fig. 7(d), the battery using Co@Fe-CNFs-1000 as the cathode produced a specific capacity of 258.4 mAh·g_{Zn}^{-1} at a current density of 2 mA·cm^{-2} (when normalized to the total mass of Zn consumed), which was superior to the Pt/C catalyst (232.1 mAh·g_{Zn}^{-1}). Solid ZABs based on Co@Fe-CNFs-1000 also show better rate performance, with a higher and more stable discharge potential when the current density is adjusted (Fig. 7e). The stability of a Co@Fe-CNFs-1000-based flexible solid-state ZABs was examined by circulating it at a current density of 1 mA·cm^{-2} (Fig. 7f). The voltage gap remained almost constant before

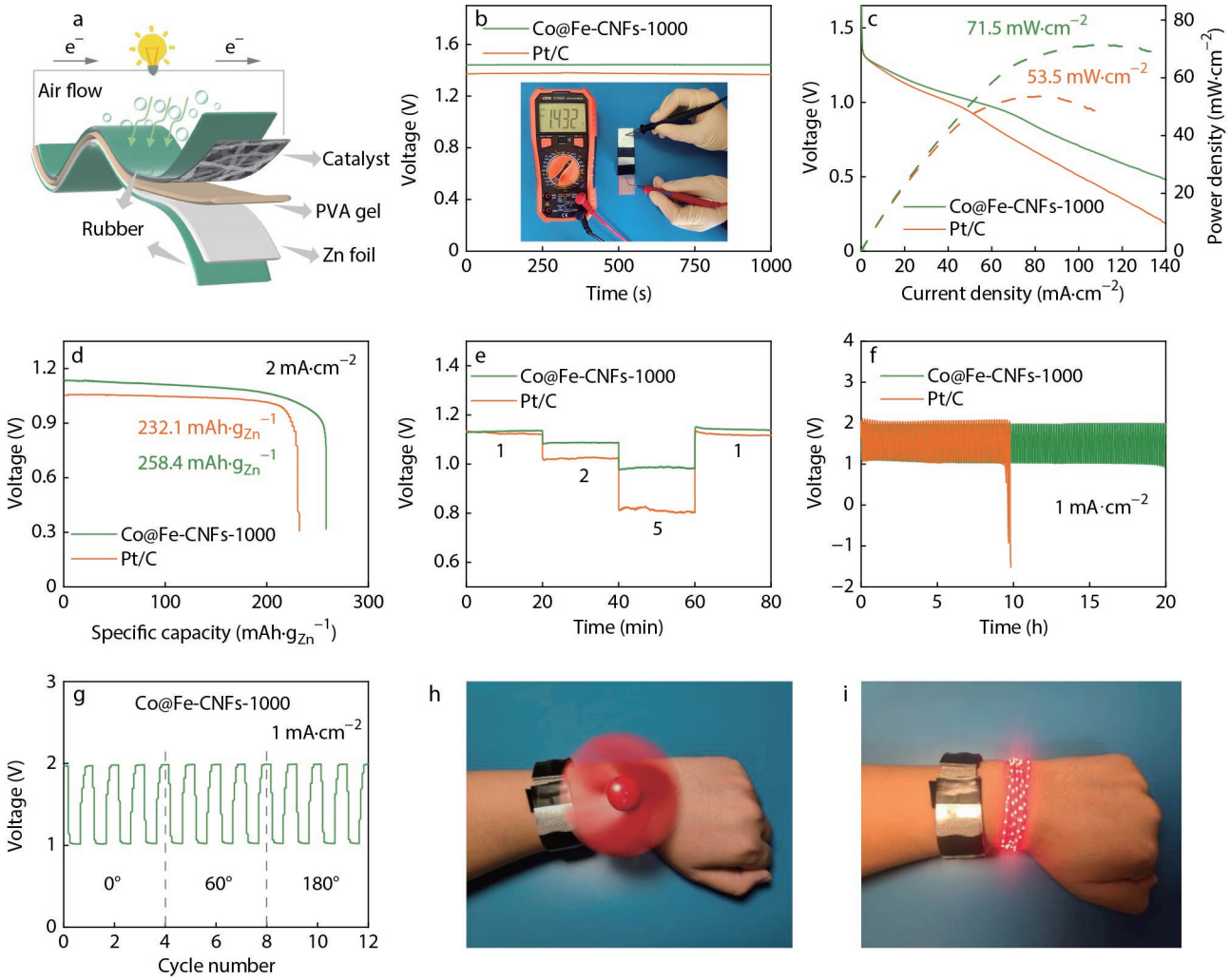

Fig. 7 (a) Schematic illustration of flexible solid-state ZABs; (b) OCV plot of flexible solid-state ZABs based on Co@Fe-CNFs-1000 and Pt/C (inset: photograph of Co@Fe-CNFs-1000-based battery); (c) Discharge polarization and corresponding power density curves; (d) The specific capacity of Co@Fe-CNFs-1000 and Pt/C air cathodes based rechargeable at a current density of 2 mA·cm^{-2}; (e) Galvanostatic discharge voltage curves at various current densities; (f) Comparison of the cycling stabilities of the flexible solid-state ZABs; (g) Cyclic stability of battery tested under different bending states at 1 mA·cm^{-2}; (h, i) Photograph of three flexible solid-state ZABs in series can drive the fan and the lamp belt to work.

https://doi.org/10.1007/s10118-023-3006-3

and after 20 h of operation. Although ZABs with Pt/C cathodes can maintain a small voltage gap during the first few hours of the cycle, the voltage gap increases dramatically at about 7 h. To evaluate these practical aspects of the battery, such as portability and flexibility, a solid ZAB was folded at different bending angles of 0°, 60° and 180° using Co@Fe-CNFs-1000 catalyst, as shown in Fig. 7(g). The results show that the battery shows good stability at 1 mA·cm^{-2}, even when folded to 180°. In addition, three separate Co@Fe-CNFs-1000-based flexible solid-state ZABs can be connected in series and easily wrapped around the wrist to provide continuous power to a red LED strip or fan (LED) (Figs. 7h and 7i).

CONCLUSIONS

In summary, Co@Fe-CNFs-1000 was successfully synthesized by mixing MOF in PAN nanofibers by electrospinning technology, combined with high temperature carbonization and electrodeposition, and was studied as a catalyst for cathode oxygen reduction reaction (ORR) of Zinc-air batteries. The catalyst Co@Fe-CNFs-1000 presents a typical one-dimensional porous fiber morphology, where Co and Fe species are coated by carbon matrix and distributed uniformly in the outer and inner layers of the fiber. Co@Fe-CNFs-1000 catalyst showed relatively excellent ORR activity, even comparable to commercial Pt/C, and showed good stability and methanol tolerance. In addition, when used as an air cathode catalyst for liquid Zinc-air batteries, it can also provide high open-circuit voltage, excellent power density, excellent specific capacity and strong charge-discharge stability. In addition, the flexible solid-state Zinc-air battery based on Co@Fe-CNFs-1000 can also show good flexibility. Therefore, this work provides novel and meaningful thinking for the construction of MOF-derived carbon-based materials for Zinc-air batteries.

Conflict of Interests

The authors declare no interest conflict.

Electronic Supplementary Information

Electronic supplementary information (ESI) is available free of charge in the online version of this article at http://doi.org/10.1007/s10118-023-3006-3.

ACKNOWLEDGMENTS

This work was financially supported by a key project of the State Key Laboratory of Bio-Fibers and Eco-Textiles of Qingdao University (No. RZ2000003348) and Major Scientific and Technological Innovation Projects of Shandong Province (No. RZ2000001594).

REFERENCES

1 Wang, H.; Su, S.; Yu, T.; Meng, C.; Zhou, H.; Zhao, W.; Yan, S.; Bian, T.; Yuan, A. FeNi/$NiFe_2O_4$ hybrids confined in N-doped carbon sponge derived from Hofmann-type MOFs for oxygen electrocatalysis. *Appl. Surf. Sci.* **2022**, *596*, 153522.

2 Ao, K.; Shi, J.; Zhang, X.; Daoud, W.A. Tuning oxygen vacancies in spinel nanosheets for binder-free oxygen cathodes with superior catalytic activity in zinc-air batteries. *J. Power Sources* **2022**, *521*, 230918.

3 Harish, K.; Balamurugan, J.; Nguyen, T. T.; Kim, N. H.; Lee, J. H. Advanced interfacial engineering of oxygen-enriched $Fe_xSn_{1-x}OSe$ nanostructures for efficient overall water splitting and flexible zinc-air batteries. *Appl. Catal. B Environ.* **2022**, *305*, 120924.

4 Zuo, H.; Zhao, Z.; He, Y.; Li, S.; Li, X.; Cheng, Z.; Cheng, C.; Thomas, A.; Liao, Y. Regulating single-atom distance in carbon electrocatalysts for efficient oxygen reduction reaction *via* conjugated microporous polymer precursors strategy. *Carbon* **2023**, *201*, 984–990.

5 Subjalearndee, N.; He, N.; Cheng, H.; Tesatchabut, P.; Eiamlamai, P.; Limthongkul, P.; Intasanta, V.; Gao, W.; Zhang, X. Gamma(*γ*)-MnO_2/rGO fibered cathode fabrication from wet spinning and dip coating techniques for cable-shaped Zn-ion batteries. *Adv. Fiber Mater.* **2022**, *4*, 457–474.

6 Liu, Y.; Chen, Z.; Zhao, N.; Tong, G.; Li, Z.; Wang, B.; Du, Y.; Pan, Q.; Li, Z.; Xie, Y.; Yang, Y. Ultra-small cobalt nanoparticles embedded into N-doped hierarchical porous carbon derived from ion-exchange MOFs as high-efficient bifunctional catalysts for rechargeable Zn-air battery. *Chem. Eng. J.* **2022**, *433*, 134469.

7 Zhu, Y.; Ning, S.; Yu, X.; Niu, X.; Chen, M.; Zhou, W.; Zhao, D.; Li, Z.; Wang, N.; Li, N.; Li, L. Cobalt nanoparticles encapsulated in iron and nitrogen co-doped urchin-like porous carbons as an efficient bifunctional oxygen reversible catalyst for Zn-air batteries. *Chem. Eng. J.* **2022**, *436*, 135191.

8 Najam, T.; Shoaib Ahmad Shah, S.; Sufyan Javed, M.; Chen, P.-T.; Chuang, C.; Saad, A.; Song, Z.; Liu, W.; Cai, X. Modulating the electronic structure of zinc single atom catalyst by P/N coordination and Co_2P supports for efficient oxygen reduction in Zn-air battery. *Chem. Eng. J.* **2022**, *440*, 135928.

9 Yu, P.; Wang, L.; Sun, F.; Xie, Y.; Liu, X.; Ma, J.; Wang, X.; Tian, C.; Li, J.; Fu, H. Co nanoislands rooted on Co-N-C nanosheets as efficient oxygen electrocatalyst for Zn-air batteries. *Adv. Mater.* **2019**, *31*, 1901666.

10 Pan, Z.; Chen, H.; Yang, J.; Ma, Y.; Zhang, Q.; Kou, Z.; Ding, X.; Pang, Y.; Zhang, L.; Gu, Q.; Yan, C.; Wang, J. $CuCo_2S_4$ nanosheets@N-doped carbon nanofibers by sulfurization at room temperature as bifunctional electrocatalysts in flexible quasi-solid-state Zn-air batteries. *Adv. Sci.* **2019**, *6*, 1900628.

11 Liu, Q.; Liu, X.; Xie, Y.; Sun, F.; Liang, Z.; Wang, L.; Fu, H. N-Doped carbon coating enhances the bifunctional oxygen reaction activity of CoFe nanoparticles for a highly stable Zn-air battery. *J. Mater. Chem. A* **2020**, *8*, 21189–21198.

12 Guo, W.; Zhang, Z.; Chen, P.; Luan, X.; Dou, J.; Bai, J.; Fang, H.; Shi, W.; Zhou, B. CMP-on-MOF bimetallic hybrids derived sheet-on-rod heterostructure as bifunctional oxygen electrocatalyst for rechargeable Zn-air batteries. *Microporous Mesoporous Mater.* **2022**, *331*, 111639.

13 Thangasamy, P.; Oh, S.; Randriamahazaka, H.; Nam, S.; Oh, I.-K. Mechanistic insight into collectively exhaustive CoPi-NPC nanosheets for oxygen reduction reaction and Zn-air battery. *Appl. Catal. B Environ.* **2022**, *316*, 121656.

14 Ma, L.; Hu, X.; Min, Y.; Zhang, X.; Liu, W.; Lam, P. K. S.; Li, M. M. J.; Zeng, R. J.; Ye, R. Microalgae-derived single-atom oxygen reduction catalysts for zinc-air batteries. *Carbon* **2023**, *203*, 827–834.

15 Wang, F.; Xiao, Z.; Liu, X.; Ren, J.; Xing, T.; Li, Z.; Li, X.; Chen, Y. Strategic design of cellulose nanofibers@zeolitic imidazolate frameworks derived mesoporous carbon-supported nanoscale $CoFe_2O_4$/CoFe hybrid composition as trifunctional electrocatalyst for Zn-air battery and self-powered overall water-splitting. *J.*

Power Sources **2022**, *521*, 230925.
16 Yang, H.; Xie, A.; Tang, Y.; Wang, Z.; Zhang, J.; Kong, L.; Song, P.; Sun, Y.; Yang, X.; Wan, P. Fe-ZIF8 coating cu foil derived carbon as a pH-universal electrocatalyst for efficient oxygen reduction reaction. *Chem. Eur. J.* **2022**, *28*, e202103275.
17 Zhai, W.; Huang, S.; Lu, C.; Tang, X.; Li, L.; Huang, B.; Hu, T.; Yuan, K.; Zhuang, X.; Chen, Y. Simultaneously integrate iron single atom and nanocluster triggered tandem effect for boosting oxygen electroreduction. *Small* **2022**, *18*, 2107225.
18 Liu, M.; Lee, J.; Yang, T. C.; Zheng, F.; Zhao, J.; Yang, C. M.; Lee, L. Y. S. Synergies of Fe single atoms and clusters on N-doped carbon electrocatalyst for pH-universal oxygen reduction. *Small Methods* **2021**, *5*, 2001165.
19 Liu, Y.; He, S.; Huang, B.; Kong, Z.; Guan, L. Influence of different Fe doping strategies on modulating active sites and oxygen reduction reaction performance of Fe,N-doped carbonaceous catalysts. *J. Energy Chem.* **2022**, *70*, 511–520.
20 Hu, Y.; Shen, T.; Zhao, X.; Zhang, J.; Lu, Y.; Shen, J.; Lu, S.; Tu, Z.; Xin, H. L.; Wang, D. Combining structurally ordered intermetallics with N-doped carbon confinement for efficient and anti-poisoning electrocatalysis. *Appl. Catal. B Environ.* **2020**, *279*, 119370.
21 Li, D.; Liang, J.; Robertson, S.J.; Chen, Y.; Wang, N.; Shao, M.; Shi, Z. Heterogeneous bimetallic organic coordination polymer-derived Co/Fe@NC bifunctional catalysts for rechargeable Li-O_2 batteries. *ACS Appl. Mater. Interfaces* **2022**, *14*, 5459–5467.
22 Zhong, B.; Zhang, L.; Yu, J.; Fan, K. Ultrafine iron-cobalt nanoparticles embedded in nitrogen-doped porous carbon matrix for oxygen reduction reaction and zinc-air batteries. *J. Colloid Interface Sci.* **2019**, *546*, 113–121.
23 Li, J.; Liu, P.; Yan, J.; Huang, H.; Song, W. Fully-conjugated covalent organic frameworks with two metal sites for oxygen electrocatalysis and Zn-air battery. *Adv. Sci.* **2023**, *10*, 2206165.
24 Zhu, X.; Zhang, J.; Wang, Y.; Yang, M.; Yu, H.; Li, T.; Hu, M.; Yang, J. Achieving high-performance oxygen reduction catalyst and Zn-air battery through a synergistic nitrogen doping strategy. *Energy Technol.* **2022**, *10*, 2200602.
25 Liu, Y.; Tu, F.; Zhang, Z.; Zhao, Z.; Guo, P.; Shen, L.; Zhang, Y.; Zhao, L.; Shao, G.; Wang, Z. Molecular scissor tailoring hierarchical architecture of ZIF-derived Fe/N/C catalysts for acidic oxygen reduction reaction. *Appl. Catal. B Environ.* **2023**, *324*, 122209.
26 Wang, T.; Gao, S.; Wei, T.; Qin, Y.; Zhang, S.; Ding, J.; Liu, Q.; Luo, J.; Liu, X. Co nanoparticles confined in mesoporous Mo/N co-doped polyhedral carbon frameworks towards high-efficiency oxygen reduction. *Chem. Eur. J.* **2023**, *29*, e202204034
27 Gao, H.; Zhu, S.; Kang, Y.; Dinh, D.A.; Hui, K. S.; Bin, F.; Fan, X.; Chen, F.; Mahmood, A.; Geng, J.; Cheong, W. C. M.; Hui, K. N. Zeolitic imidazolate framework-derived Co-Fe@NC for rechargeable hybrid sodium-air battery with a low voltage gap and long cycle life. *ACS Appl. Energy Mater.* **2022**, *5*, 1662–1671.
28 Song, K.; Feng, Y.; Zhou, X.; Qin, T.; Zou, X.; Qi, Y.; Chen, Z.; Rao, J.; Wang, Z.; Yue, N.; Ge, X.; Zhang, W.; Zheng, W. Exploiting the trade-offs of electron transfer in MOF-derived single Zn/Co atomic couples for performance-enhanced zinc-air battery. *Appl. Catal. B Environ.* **2022**, *316*, 121591.
29 Yu, K.; Shi, P. H.; Fan, J. C.; Min, Y. L.; Xu, Q. J. Porous Fe, Co, and N-co-doped carbon nanofibers as high-efficiency oxygen reduction catalysts. *J Nanopart Res* **2019**, *21*, 230.
30 Zhang, Y.; He, Q.; Chen, Z.; Chi, Y.; Sun, J.; Yuan, D.; Zhang, L. Hierarchically porous Co@N-doped carbon fiber assembled by MOF-derived hollow polyhedrons enables effective electronic/mass transport: an advanced 1D oxygen reduction catalyst for Zn-air battery. *J. Energy Chem.* **2023**, *76*, 117–126.
31 Niu, Q.; Chen, B.; Guo, J.; Nie, J.; Guo, X.; Ma, G. Flexible, porous, and metal-heteroatom-doped carbon nanofibers as efficient ORR electrocatalysts for Zn-air battery. *Nanomicro Lett.* **2019**, *11*, 8.
32 Liu, X.; Zhang, Y.; Zhao, Z.; Gao, H.; Kang, J.; Wang, R.; Ge, G.; Jia, X. Highly exposed discrete Co atoms anchored in ultrathin porous N,P-codoped carbon nanosheets for efficient oxygen electrocatalysis and rechargeable aqueous/solid-state Zn-air batteries. *J. Mater. Chem. A* **2021**, *9*, 22643–22652.
33 Zhao, H. L.; Wu, S.; Liu, C. Y.; Yan, X. T.; Xu, X.; Fu, S. S.; Wang, Y. B.; Su, Q.; Wang, X.; Yang, Q. L. Encapsulation Fe-N_x combined with Co@C to construct efficient oxygen reduction catalysts with bimetallic sites and the application of Zn-air batteries. *Mater. Today Chem.* **2022**, *26*, 101174.
34 Li, G.; He, X.; Yin, F.; Chen, B.; Yin, H. Co-Fe/MIL-101(Cr) hybrid catalysts: preparation and their electrocatalysis in oxygen reduction reaction. *Int. J. Hydrog. Energy* **2019**, *44*, 11754–11764.
35 Chen, X. L.; Huang, J. W.; Huang, Y. C.; Du, J.; Jiang, Y. F.; Zhao, Y.; Zhu, H. B. Efficient Fe-Co-N-C electrocatalyst towards oxygen reduction derived from a cationic Co^{II}-based metal-organic framework modified by anion-exchange with potassium ferricyanide. *Chem. Asian J.* **2019**, *14*, 995–1003.
36 Zhang, Z.; Jin, H.; Zhu, J.; Li, W.; Zhang, C.; Zhao, J.; Luo, F.; Sun, Z.; Mu, S. 3D flower-like ZnFe-ZIF derived hierarchical Fe,N-codoped carbon architecture for enhanced oxygen reduction in both alkaline and acidic media, and zinc-air battery performance. *Carbon* **2020**, *161*, 502–509.
37 Xue, Y.; Guo, Y.; Zhang, Q.; Xie, Z.; Wei, J.; Zhou, Z. MOF-derived Co and Fe species loaded on N-doped carbon networks as efficient oxygen electrocatalysts for Zn-air batteries. *Nanomicro Lett.* **2022**, *14*, 162.
38 Shen, M.; Lin, X.; Xi, W.; Yin, X.; Gao, B.; He, L.; Zheng, Y.; Lin, B. Mesoporous waffle-like N-doped carbon with embedded Co nanoparticles for efficiently electrocatalytic oxygen reduction and evolution. *J. Colloid Interface Sci.* **2023**, *633*, 374–382.
39 Guo, S.; Wang, J.; Sun, Y.; Peng, L.; Li, C. Interface engineering of Co_3O_4/CeO_2 heterostructure *in-situ* embedded in Co/N-doped carbon nanofibers integrating oxygen vacancies as effective oxygen cathode catalyst for Li-O_2 battery. *Chem. Eng. J.* **2023**, *452*, 139317.
40 Al-Zoubi, T.; Zhou, Y.; Yin, X.; Janicek, B.; Sun, C.; Schulz, C. E.; Zhang, X.; Gewirth, A. A.; Huang, P.; Zelenay, P.; Yang, H. Preparation of nonprecious metal electrocatalysts for the reduction of oxygen using a low-temperature sacrificial metal. *J. Am. Chem. Soc.* **2020**, *142*, 5477–5481.
41 Peera, S. G.; Balamurugan, J.; Kim, N. H.; Lee, J. H. Sustainable synthesis of Co@NC core shell nanostructures from metal organic frameworks *via* mechanochemical coordination self-assembly: an efficient electrocatalyst for oxygen reduction reaction. *Small* **2018**, *14*, 1800441.
42 Zheng, Q.; Xiong, Y.; Tang, K.; Wu, M.; Hu, H.; Zhou, T.; Wu, Y.; Cao, Z.; Sun, J.; Yu, X.; Wu, C. Modulation of pore-size in N,S-codoped carbon/Co_9S_8 hybrid for a stronger O_2 affinity toward rechargable zinc-air battery. *Nano Energy* **2022**, *92*, 106750.
43 Long, J.; Zhou, D.; Chen, C.; Shen, K. Structural and interface engineering of Co nanocatalysts induce boosting the electrochemical performance for rechargeable zinc-air battery. *Appl. Surf. Sci.* **2022**, *602*, 154304.
44 Meng, D.; Zhang, C.; Liang, Y.; Qiu, W.; Kong, F.; He, X.; Chen, M.; Liang, P.; Zhang, Z. Electrospun cobalt prussian blue analogue-derived nanofibers for oxygen reduction reaction and lithium-ion batteries. *J. Colloid Interface Sci.* **2021**, *599*, 280–290.
45 Yang, H.; Hu, S.; Zhao, H.; Luo, X.; Liu, Y.; Deng, C.; Yu, Y.; Hu, T.; Shan, S.; Zhi, Y.; Su, H.; Jiang, L. High-performance Fe-doped ZIF-8 adsorbent for capturing tetracycline from aqueous solution. *J. Hazard. Mater.* **2021**, *416*, 126046.
46 Zhang, Y.; Chen, Z.; Tian, J.; Sun, M.; Yuan, D.; Zhang, L. Nitrogen doped $CuCo_2O_4$ nanoparticles anchored on beaded-like carbon

nanofibers as an efficient bifunctional oxygen catalyst toward zinc-air battery. *J. Colloid Interface Sci.* **2022**, *608*, 1105–1115.
47 Bai, Q.; Shen, F. C.; Li, S. L.; Liu, J.; Dong, L. Z.; Wang, Z. M.; Lan, Y. Q. Cobalt@nitrogen-doped porous carbon fiber derived from the electrospun fiber of bimetal-organic framework for highly active oxygen reduction. *Small Methods* **2018**, *2*, 1800049.
48 He, H.; Lei, Y.; Liu, S.; Thummavichai, K.; Zhu, Y.; Wang, N. Tunable active-sites of Co nanoparticles encapsulated in carbon nanofiber as high performance bifunctional OER/ORR electrocatalyst. *J. Colloid Interface Sci.* **2023**, *630*, 140–149.
49 Hung, K. Y.; Hosseini, S.; Ko, T. E.; Tseng, C. M.; Li, Y. Y. Highly efficient rechargeable Zn-air batteries based on hybrid CNT-grafted, Co/CoS_2-Fe embedded, Nitrogen-doped porous carbon nano-frameworks. *Fuel* **2022**, *316*, 123328.
50 Du, L.; Gao, X. Y.; Li, Z.; Wang, G. Y.; Wen, Z.; Yang, C. C.; Jiang, Q. Metal-organic frameworks derived Co/N-doped carbon nanonecklaces as high-efficient oxygen reduction reaction electrocatalysts. *Int. J. Hydrog. Energy* **2022**, *47*, 39133–39145.
51 Hu, Z.; Dong, S.; He, Q.; Chen, Z.; Yuan, D. Synergetic nanostructure engineering and electronic modulation of a 3D hollow heterostructured $NiCo_2O_4$@NiFe-LDH self-supporting electrode for rechargeable Zn-air batteries. *Inorg. Chem.* **2023**, *62*, 7471–7482.
52 Jafari, M.; Gharibi, H.; Parnian, M. J. Metal organic framework derived iron-nitrogen doped porous carbon support decorated with cobalt and iron as efficient nanocatalyst toward oxygen reduction reaction. *J. Power Sources* **2021**, *499*, 229956.
53 Sun, X.; Wei, P.; Zhang, J.; Gu, S.; Yang, R.; Fang, C.; Li, Q.; Han, J.; Jiang, Z.; He, J. P,N-codoped carbon nanofibers confined ultra-small bimetallic NiCoP for highly efficient overall water splitting. *Appl. Surf. Sci.* **2021**, *570*, 151247.
54 Niu, Y.; Teng, X.; Gong, S.; Xu, M.; Sun, S. G.; Chen, Z. Engineering two-phase bifunctional oxygen electrocatalysts with tunable and synergetic components for flexible Zn-air batteries. *Nanomicro Lett.* **2021**, *13*, 126.
55 Li, K.; Zhang, Y.; Wang, P.; Long, X.; Zheng, L.; Liu, G.; He, X.; Qiu, J. Core-Shell ZIF-67@ZIF-8-derived multi-dimensional cobalt-nitrogen doped hierarchical carbon nanomaterial for efficient oxygen reduction reaction. *J. Alloy. Compd.* **2022**, *903*, 163701.
56 Li, G.; Deng, W.; He, L.; Wu, J.; Liu, J.; Wu, T.; Wang, Y.; Wang, X. Zn, Co, and Fe tridoped N–C core-shell nanocages as the high-efficiency oxygen reduction reaction electrocatalyst in zinc-air batteries. *ACS Appl. Mater. Interfaces* **2021**, *13*, 28324–28333.

https://doi.org/10.1007/s10118-023-3006-3